Stochastic Geometry Based Performance Analysis of Terrestrial-to-Aerial Networks for Nomadic Communications

Wen-Yu Dong, Shaoshi Yang, *Senior Member, IEEE*, Wei Lin, Wei Zhao, Jia-Xing Gui, Ping Zhang, *Fellow, IEEE*, and Sheng Chen, *Life Fellow, IEEE*

***Abstract*—In this paper, we propose a stochastic geometry based innovative model to characterize the impact of the limited-size distribution region of terrestrial terminals in terrestrial-to-aerial networks by jointly using a binomial point process (BPP) and a type-II Matérn hard-core point process (MHCPP). Then, we analyze the relationship between the spatial distribution of the coverage areas of aerial nodes and the limited-size distribution region of terrestrial terminals, thereby deriving the distance distribution of the terrestrial-aerial (T-A) links. Furthermore, we consider the stochastic nature of the spatial distributions of terrestrial terminals and unmanned aerial vehicles (UAVs), and conduct a thorough analysis of the coverage probability of the T-A links under Nakagami fading. Finally, the accuracy of our theoretical derivations are confirmed by Monte Carlo simulations. Our research offers fundamental insights into the system-level performance optimization for the realistic terrestrial-to-aerial networks involving nomadic aerial base-stations and terrestrial terminals confined in a limited-size region.**

***Index Terms*—Terrestrial-to-aerial networks, stochastic geometry, nomadic communications, coverage probability.**

I. Introduction

Employing UAVs as aerial base-stations (BSs) is regarded as a promising solution that can provide flexible communication and address capital and operational cost issues for unexpected and temporary needs such as hotspots and disaster relief operations [1]. Compared to traditional ground-based networks, UAVs not only offer greater coverage and increased line-of-sight opportunities, but also provide cost-effectiveness and enhanced adaptability. To fully characterize and better understand the performance of UAV networks, it is essential to study the static and dynamic components of the wireless environment and to develop appropriate solutions [2].

In this context, many studies on the performance analysis of terrestrial-to-aerial networks have been proposed. Particularly, a unified expression for the coverage probability is derived, for both millimeter wave (mmWave) and sub-6 GHz scenarios, in [3]. The authors of [4] investigate a unified framework for 3-hop UAV-assisted non-orthogonal multipleaccess (NOMA) networks. The work in [5] analyzes the end-to-end performance of a UAV-assisted data ferrying network where the UAV serves as a data ferry between the source BS and multiple destination receivers. In [6], the authors analyze ground-to-UAV communications by considering that the distribution of UEs follows the Poisson Cluster process (PCP) and each UAV is dedicated to a specific cluster.

In various real-world scenarios, such as post-disaster urban reconstruction, it is commonly seen that users tend to congregate in limited-size areas. Understanding this fundamental property is critical for more effective network restoration or achieving more efficient network operation. Nevertheless, evidently a significant gap exists in the current research landscape regarding the performance analysis of terrestrial-to-aerial networks, whose terrestrial terminals are located in limited-size regions. Existing studies often model terrestrial terminals by a Poisson point process (PPP) or a PCP that both rely on assuming an infinite distribution region [3–6]. The main motivation of our work is to address this void in the research concerning terrestrial-to-aerial networks.

Inspired by the insights gained from prior discoveries, this study directs its focus towards the performance of terrestrial-to-aerial networks, whose terrestrial terminals are constrained in limited-size regions. This issue is challenging and crucial for nomadic communication. Our contributions are summarized as follows. i) We introduce an innovative terrestrial-to-aerial network system tailored to a limited-size region of terrestrial terminals by jointly using a binomial point process (BPP) [7] and a type-II Matern hard-core point process (MHCPP) [8]. ii) We analyze the sophisticated relationship between the spatial distribution of the coverage areas of aerial nodes and the limited-size distribution region of terrestrial terminals, thereby deriving the T-A links' distance distribution and further analyzing the coverage probability (CP). iii) We garner a substantial volume of results to assess the performance of the terrestrial-to-aerial network considered via extensive Monte Carlo simulations, which demonstrate the correctness of our theoretical analysis.

II. System Model

The system model proposed is depicted in Fig. 1, which consists of a group of aerial nodes, (A_n, $n \in \{1, \cdots, N_A\}$ and $N_A \geq 1$) and a number of terrestrial terminals, (T_l, $l \in \{1, \cdots, N_0\}$ and $N_0 \geq 1$). Every aerial node is equipped with an antenna array that supports beamforming, while each terrestrial terminal has a single antenna. Both the aerial nodes and terrestrial terminals work in half-duplex mechanisms.

It is assumed that aerial nodes in this system fly at the same height H_A above the earth surface. For the sake of conciseness, we also use A or AN and T or TN to stand for aerial node and terrestrial node, respectively.

W.-Y. Dong, S. Yang, W. Lin, W. Zhao, J.-X Gui and P. Zhang are with the School of Information and Communication Engineering, Beijing University of Posts and Telecommunications, with the Key Laboratory of Universal Wireless Communications, Ministry of Education, and also with the State Key Laboratory of Networking and Switching Technology, Beijing 100876, China (E-mails: wenyu.dong@bupt.edu.cn, shaoshi.yang@bupt.edu.cn, linwei@bupt.edu.cn, wei.zhao@bupt.edu.cn, jiaxing.gui@bupt.edu.cn, pzhang@bupt.edu.cn).

S. Chen is with the School of Electronics and Computer Science, University of Southampton, Southampton SO17 1BJ, U.K. (E-mail: sqc@ecs.soton.ac.uk).

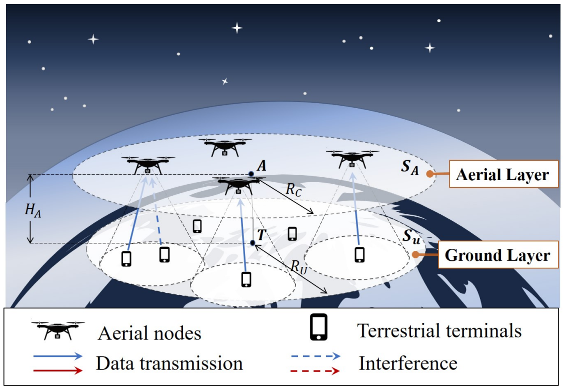

Fig. 1. Illustration of the terrestrial-to-aerial network system.

A. Topology Deployment

1) Deployment of TNs: We consider a realistic scenario where the majority of users are geographically concentrated within a specific finite region. To represent this user concentration, we use a circular bounded area designated as $\mathcal{S}_{\mathcal{U}}$, with radius R_U. In a limited-size area, points near the boundary are spatially limited, which may result in the distribution of points being inconsistent with the assumptions of PPP spatial uniformity and independence. Thus, within this area, users are modeled as BPP denoted as Φ_1, with density λ_T, which can effectively describe the distribution of points within a limited-size area. Additionally, users located inside the coverage area of an AN also adhere to the BPP, represented as Φ_U, with density λ_T.

2) Deployment of ANs: In order to reduce the overlap of ANs' coverage areas on the ground, we exploit type-II MHCPP with exclusivity to mimic the deployment of ANs. Due to the modeling premise of MHCPP being within a limited-size area, it can adapt well to the characteristics of the limited-size area. The aerial nodes are randomly dispersed in the circular plane, denoted as $\mathcal{S}_{\mathcal{A}}$, with radius R_C. The vertical distance from the ANs to the ground is H_A. Additionally, the coverage of each AN A can be modeled as a conical shape with a ground circular plane of radius R_A. That is, the coverage range of AN A on the ground is the circular region $\mathcal{S}_{\mathcal{A}}^{'} = \mathcal{B}(\boldsymbol{a}, R_A)$, which contains TNs capable of establishing connection with the AN, where $\boldsymbol{a}$ is the ground projection position of A. Given that there is a strong repulsion among the points in the MHCPP. We set the ground coverage radius of AN R_A to half of the radius of the repulsive space between ANs. Hence, TNs can establish communication with at most one AN.

B. Terrestrial-Aerial Link Propagation Model

1) Channel Fading: The aerial-terrestrial connection is commonly relying on line-of-sight (LoS) transmission but it may encounter obstacles such as buildings or plants that impede its signal propagation [9]. It is worth noting that Nakagami-m small-scale fading is accurate for characterizing the impact of different propagation paths on signal strength, especially in environments with numerous obstacles. Specifically, the small-scaling channel fading coefficient h_{TA} of T-A link exhibits Nakagami fading. Consequently, $|h_{TA}|^2$ can be modeled as a random variable that follows a normalized Gamma distribution. The Nakagami fading parameter is denoted by N_{TA}, and for the sake of simplicity, it is assumed to be a positive integer.

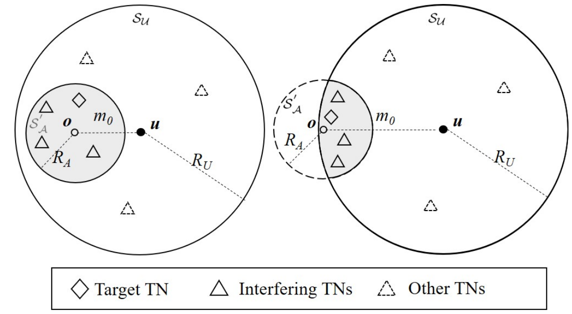

Fig. 2. The positional relationship between $\mathcal{S}_{\mathcal{A}}^{'}$ and $\mathcal{S}_{\mathcal{U}}$, where $\boldsymbol{o}$ is the ground projection position of the AN considered.

2) SINR model: The SINR at the AN receiver A of the T-A link from the target transmitter T_m can be expressed as:

$$\begin{aligned}\mathrm{SINR}_1 &= \frac{P_T \left|h_{T_m A}\right|^2 (H_A^2 + R_m^2)^{-\frac{\alpha_1}{2}}}{I_T + \sigma_T^2} \\ &\approx \frac{P_T \left|h_{T_m A}\right|^2 (H_A^2 + R_m^2)^{-\frac{\alpha_1}{2}}}{I_T},\end{aligned} \tag{1}$$

where $I_T = \sum_{T_n \in \Phi_U \setminus T_m} P_T \left|h_{T_n}\right|^2 (H_A^2 + R_n^2)^{-\frac{\alpha_1}{2}}$, $\Phi_U = \Phi_1 \bigcap \mathcal{B}(\boldsymbol{a}, R_A)$, T_n are the interfering TNs, P_T is the transmit power at TNs, R_m and R_n are the distances from the target node T_m and the interference node T_n to the terrestrial projection position $\boldsymbol{a}$ of the AN A, respectively, while α_1 is the path-loss exponent of the T-A link, and σ_T^2 is the strength of additive white Gaussian noise (AWGN) of the T-A link. The approximation in (1) is due to the fact that the system is interference limited and $I_T \gg \sigma_T^2$.

III. Distribution of Distances

In order to derive the coverage probability expressions, it is necessary to firstly characterize the distance distributions arising from the stochastic geometry of the system under consideration. In particular, we present the PDF for the distribution of distances in **Lemma 1** and **Lemma 2**.

From Fig. 1, it can be seen that the coverage area of each AN is limited-size, impacting the users eligible to establish communication with an AN. Specifically, these users must be situated inside the intersecting region of $\mathcal{S}_{\mathcal{A}}^{'}$ and $\mathcal{S}_{\mathcal{U}}$. Given the constant vertical separation between ANs and the ground, our focus narrows down to the distribution of the distance r between the user and the AN's projection point on the ground. Let the random variable M be the distance from the projected location of an AN to the center of the user area. In this context, we can analyze the PDF of the distance r conditioned on M equal to m_0. Based on the geometric relationships, it becomes apparent that when $M > R_A + R_U$, there will be no users within the AN's coverage range. Thus, we assume that the radius R_C of all the ANs' location area, $\mathcal{S}_{\mathcal{A}}$, is equivalent to the sum of R_A and R_U, i.e., $R_C = R_A + R_U$.

$$\mathcal{L}_{I_T}(s)=\begin{cases}\mathcal{L}_{I_1}(s)=\sum\limits_{n_I=1}^{N_0-1}\binom{N_0-1}{n_I}\dfrac{R_A^{2n_I}\left(R_U^2-R_A^2\right)^{N_0-1-n_I}}{R_U^{2(n_I+1)}}\left(\displaystyle\int_0^{R_A}D_2\,\frac{2r_n}{R_A^2}\mathrm{d}r_n\right)^{n_I}, & 0<m_0<R_U-R_A,\\ \mathcal{L}_{I_2}(s)=\sum\limits_{n_I=1}^{N_0-1}\binom{N_0-1}{n_I}\dfrac{\gamma^{n_I}\left(R_U^2-\gamma\right)^{N_0-1-n_I}}{R_U^{2(n_I+1)}} & \\ \qquad\times\left(\displaystyle\int_{R_U-m_0}^{R_A}D_2\frac{2\pi r}{\gamma}\mathrm{d}r_n+\int_{R_U-m_0}^{R_A}D_1D_2\mathrm{d}r_n\right)^{n_I}, & R_U-R_A<m_0<R_U,\\ \mathcal{L}_{I_3}(s)=\sum\limits_{n_I=1}^{N_0-1}\binom{N_0-1}{n_I}\dfrac{\gamma^{n_I}(R_U^2-\gamma)^{N_0-1-n_I}}{R_U^{2(n_I+1)}}\left(\displaystyle\int_{m_0-R_U}^{R_A}D_1D_2\,\mathrm{d}r_n\right)^{n_I}, & R_U<m_0<R_U+R_A.\end{cases}\tag{9}$$

The PDF of the distance distribution from the users to the ground projection point of an AN can be categorized into two scenarios based on the relative spatial relationship between the coverage range of the AN, $\mathcal{S}_{\mathcal{A}}^{'}$, and the user area, $\mathcal{S}_{\mathcal{U}}$. These two scenarios are illustrated in Fig. 2.

Lemma 1. *The PDF describing the distance r between a given TN and the projected location of the AN within the overlapping area of $\mathcal{S}_{\mathcal{A}}^{'}\bigcap\mathcal{S}_{\mathcal{U}}$, conditioned on $M=m_0$, is expressed as:*

$$f_R(r|m_0)=\begin{cases}f_{R^{1)}}(r|m_0)=\frac{2r}{R_A^2}, & 0<r<R_A \text{ and } 0<m_0<R_U-R_A,\\ f_{R^{2)}}(r|m_0)=\frac{2\pi r}{\gamma}, & 0<r<R_U-m_0 \text{ and } R_U-R_A<m_0<R_U,\\ f_{R^{3)}}(r|m_0), & R_U-m_0<r<R_A \text{ and } R_U-R_A<m_0<R_U,\\ f_{R^{3)}}(r|m_0), & m_0-R_U<r<R_A \text{ and } R_U<m_0<R_U+R_A,\end{cases}\tag{2}$$

where $f_{R^{3)}}(r|m_0)=\frac{r\sqrt{4m_0^2R_U^2-\left(m_0+R_U^2-r^2\right)^2}}{m_0^2}+2r\left(\varphi_3-\frac{1}{2}\sin\left(2\varphi_3\right)\right)+\frac{\left(m_0^2+R_U^2-r^2\right)\sqrt{2R_U^2(m_0+r^2)-R_U^4-(m_0^2-r^2)^2}}{2m_0^2r}$, $\gamma=R_U^2\left(\theta_2-\frac{1}{2}\sin\left(2\theta_2\right)\right)+R_A^2\left(\varphi_2-\frac{1}{2}\sin\left(2\varphi_2\right)\right)$, $\theta_2=\arccos\left(\frac{m_0+R_U^2-R_A^2}{2m_0R_U}\right)$, $\varphi_2=\arccos\left(\frac{m_0+R_A^2-R_U^2}{2m_0R_A}\right)$, *and* $\varphi_3=\arccos\left(\frac{m_0^2-R_U^2+r^2}{2m_0r}\right)$.

Proof. See Appendix A. □

Remark 1. *Due to the independent and uniform distribution of TNs within the overlapping area, it can be observed that when the distance between the projection point and the center of the user area is $M=m_0$, the distance variables r_m and r_n for the target TN and interference TNs are independently and identically distributed. Specifically, this can be expressed as $f_{R_m}(r_m|m_0)=f_{R_n}(r_n|m_0)=f_R(r|m_0)$.*

Lemma 2. *The PDF of the distance M from the projection point of the AN to the center of the user area is given by*

$$f_M(m_0)=\frac{2m_0}{\left(R_A+R_U\right)^2},\ 0<m_0<R_A+R_U.\tag{10}$$

Proof. Considering that the movement range of the projection point is within $\mathcal{B}(\boldsymbol{u},R_U)$, the range of the distance m_0 from the projection point to the center of the user area $\mathcal{S}_{\mathcal{U}}$ is $0<m_0<R_U+R_A$. Thus the CDF of M can be expressed as

$$F_M(m_0)=\frac{m_0^2}{\left(R_A+R_U\right)^2},\ 0<m_0<R_A+R_U.\tag{11}$$

The corresponding PDF can be derived by differentiating (11) with respect to m_0. This completes the proof. □

IV. Performances Analysis

In this section, we conduct an analysis on the coverage probabilities for the T-A link link, assuming that at least one user is in $\mathcal{S}_{\mathcal{A}}^{'}$. The coverage probability refers to the likelihood that the SINR at the receiver is larger than the minimum SINR threshold necessary for successful data transmission.

Theorem 1. *The coverage probability of a TN communicating with an AN within the coverage range of the AN under the Nakagami fading channel is given by*

$$\begin{aligned}P_{\mathrm{cov}}^{T-A}&\triangleq\mathbb{P}(\mathrm{SINR}_1\geq T_{h_1})\\&=\int\int\sum_{n=1}^{N_{TA}}(-1)^{n+1}\binom{N_{TA}}{n}\mathbb{E}_I\left[\exp\left(-sI_T\right)\right]\\&\quad\times f_{R_m}(r_m|m_0)\,f_M(m_0)\,\mathrm{d}r_m\,\mathrm{d}m_0,\end{aligned}\tag{5}$$

where T_{h_1} is the SINR threshold of the T-A link, $\mathbb{E}_I\left[\exp\left(-sI_T\right)\right]=\mathcal{L}_{I_T}(s)$, is the Laplace transform of the cumulative interference power I_T, $s=\frac{n\eta T_{h_1}(H_A^2+r_m^2)^{\frac{\alpha_1}{2}}}{P_T}$ with $\eta=N_{TA}(N_{TA}!)^{-\frac{1}{N_{TA}}}$, and N_{TA} is Nakagami fading parameter.

Proof. See Appendix B. □

Lemma 3. *Laplace transform of random variable I_T is*

$$\mathcal{L}_{I_T}(s)=\mathbb{E}_{N_I,R_n}\Bigg[\prod_{T_n\in\Phi_U\setminus T_m}\underbrace{\left(1+\frac{sP_T}{N_{TA}(H_A^2+r_n^2)^{\frac{\alpha_1}{2}}}\right)^{-N_{TA}}}_{D_2}\Bigg],\tag{6}$$

where the expectation is over the number of interference users N_I and the interfering users' distances R_n.

Proof. See Appendix C. □

The point distribution of the interference users can be described by a BPP. Therefore, the number of interference users

N_I follows a binomial distribution with a certain probability of success. The probability of success can be expressed as

$$P_I = \begin{cases} P_{I_1} = \frac{R_A^2}{R_U^2}, & 0 < m_0 < R_U - R_A, \\ P_{I_2} = \frac{\gamma}{R_U^2}, & R_U - R_A < m_0 < R_U + R_A. \end{cases} \tag{7}$$

Noting the PDF $f_R(r_n|m_0)$ (2), we obtain the three expressions of $\mathcal{L}_{I_T}(s)$ in the three different ranges of $0 < m_0 < R_U - R_A$, $R_U - R_A < m_0 < R_U$ and $R_U < m_0 < R_U + R_A$, which are given in (9) at the top of the page, where N_0 is the total number of users, and $D_1 = f_{R^{3)}}(r_n|m_0)$.

$\mathcal{L}_{I_1}(s)$ for $0 < m_0 < R_U - R_A$ is derived as follows:

$$\mathcal{L}_{I_1}(s) = \sum_{n_I=1}^{N_0-1} \binom{N_0-1}{n_I} \frac{R_A^{2n_I}(R_U^2 - R_A^2)^{N_0-1-n_I}}{R_U^{2(n_I+1)}} \times \left(\int_0^{R_A} D_2 \frac{2r_n}{R_A^2} \mathrm{d}r_n \right)^{n_I}. \tag{8}$$

Applying a similar approach, we can derive the expressions for $\mathcal{L}_{I_2}(s)$ and $\mathcal{L}_{I_3}(s)$ as given in (9).

By substituting (2), (10) and (9) into (5), we obtain the coverage probability $P_{\text{cov}}^{T\text{-}A}$ of the terrestrial-aerial link.

V. Numerical Results

In this section, we verify the derived analytical expressions using Monte Carlo simulations with 50,000 runs. The results from the analytical derivations of Section IV are indicated in the following figures as 'Analysis', while the Monte Carlo results are indicated in the figures as 'Simulation'. Unless otherwise specifically stated, the default system parameters utilized in the simulations are listed in Table I.

TABLE I
DEFAULT SIMULATION SYSTEM PARAMETERS.

Notation	Parameters	Values
H_A	Height of ANs	0.05 km
R_U, R_A	Radius of $\mathcal{S}_\mathcal{U}$ and $\mathcal{S}_A^{'}$	9.5 km, 0.5 km
P_T	Power of transmitters in *TN*	20 dBw
λ_T	Density of terrestrial nodes	10^{-4}
N_{TA}	Nakagami fading parameter	3
α_1	Path-loss exponents of T-A link	2
T_{h_1}	SINR threshold of the T-A link	variable

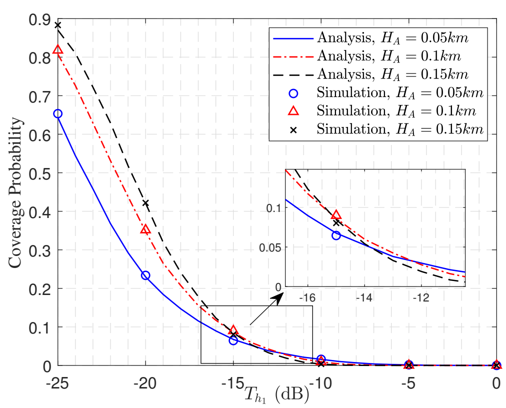

Fig. 3. Coverage probability of terrestrial-aerial link as the function of SINR threshold T_{h_1} given three different H_A.

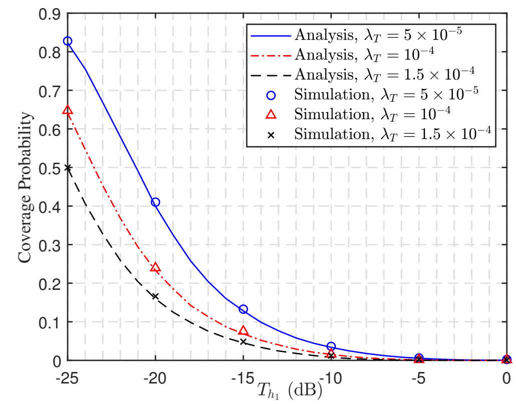

Fig. 4. Coverage probability of terrestrial-aerial link as the function of SINR threshold T_{h_1} given three different λ_T.

Fig. 3 depicts the coverage probability as the function of the SINR threshold T_{h_1}, given three different values of the height of the ANs H_A. It can be seen from Fig. 3 that increasing the SINR threshold T_{h_1} decreases the coverage probability, i.e., decreasing the likelihood of experiencing the link coverage. This is expected due to the inverse relationship between T_{h_1} and the probability of achieving an SINR that surpasses the given threshold value. Notably, the results of Fig. 3 indicates that increasing the height of ANs enhances the coverage probability of the T-A link. This can be explained

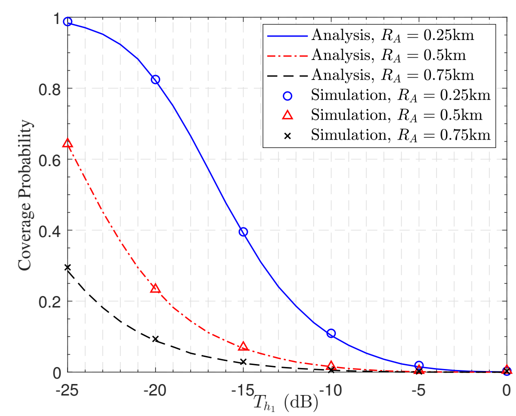

Fig. 5. Coverage probability of terrestrial-aerial link as the function of SINR threshold T_{h_1} given three different R_A.

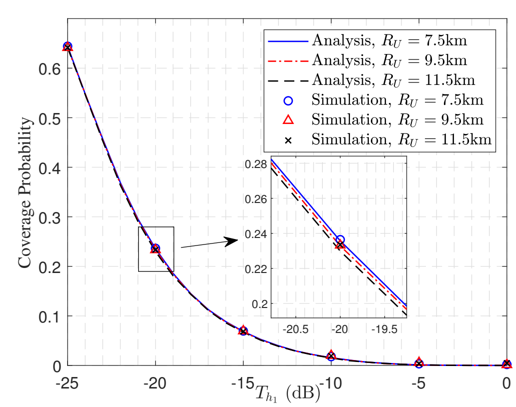

Fig. 6. Coverage probability of terrestrial-aerial link as the function of SINR threshold T_{h_1} given three different R_U.

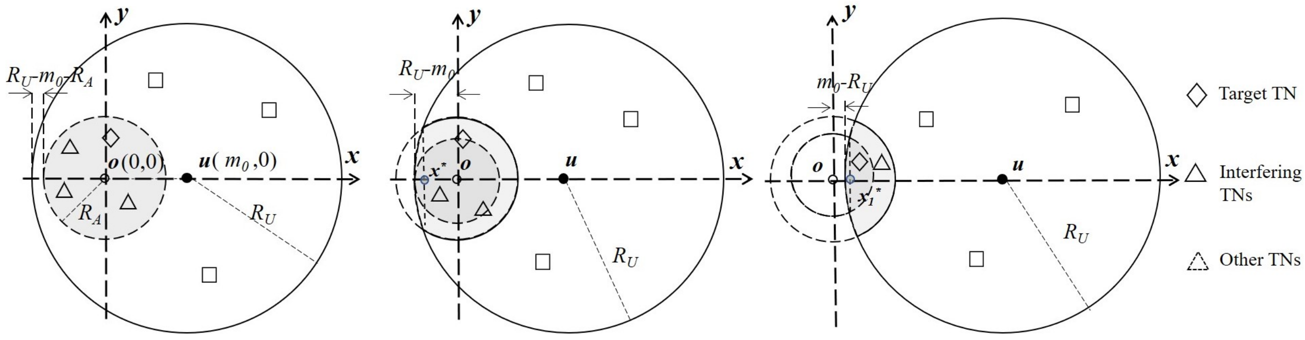

(a) $0 < m_0 < R_U - R_A$ (b) $R_U - R_A < m_0 < R_U$ (c) $R_U - R_A < m_0 < R_U + R_A$

Fig. 7. Illustration of positional relationships under different conditions.

by examining the impact of H_A on the SINR. From the SINR (1) of the T-A link and the accumulative interference power (II-B2) of the link, it is clear that the reduction in the MUI is far more than the reduction in the target signal power when increasing H_A. Therefore, increasing H_A increases the link SINR, leading to the enhancement of the coverage probability.

Fig. 4 investigates the impact of the density of terrestrial nodes λ_T on the achievable coverage probability performance. It can be seen from Fig. 4 that increasing the the density of terrestrial nodes reduces the achievable coverage probability. This is because a higher λ_T indicates a higher number of terrestrial transmitters concurrently attempting to access the UAV, leading to a higher MUI and consequently a lower coverage probability.

Fig. 5 portrays the coverage probability as the function of the SINR threshold T_{h_1}, given three different values of the AN's ground coverage radius R_A, where the influence of R_A on the achievable coverage probability is clearly exhibited. Specifically, increasing the AN's ground coverage radius leads to noticeably reduction in the coverage probability. This is because a larger ground region $\mathcal{S}_{\mathcal{A}}^{'}$ covers more terrestrial nodes, which can communicate with the same AN. This results in a higher number of territorial transmitters concurrently attempting to access the AN, leading to a higher MUI and consequently a lower coverage probability.

Fig. 6 studies the influence of the radius R_U on the coverage probability, indicating that impact of R_U on the coverage probability is negligible. Increasing R_U increases the area $\mathcal{S}_{\mathcal{U}}$ of terrestrial nodes but this hardly changes the number of the TNs within the AN's coverage area $\mathcal{S}_{\mathcal{A}}^{'}$, given the same user density λ_T. That is, the number of ground nodes connected to the same AN is hardly changed. Consequently, the MUI of the T-A link is hardly changed and the coverage probability is hardly affected, when R_U is changed.

VI. Conclusions

In this paper, we have proposed a tractable approach for analyzing the coverage probability of T-A links in a terrestrial-to-aerial network, whose terrestrial terminals are located in a limited-size region. This condition incurs significant challenge for the performance analysis. Utilizing the expressions of coverage probability derived under various conditions, we can input relevant parameter values in analogous scenarios to determine the coverage probability of the end-to-end links between the terrestrial terminals and the UAVs. Furthermore, with these theoretical results, we can gain a clear understanding of the impact imposed by critical system parameters. Therefore, our study offers theoretical guidance and valuable insights on how to conduct terrestrial-to-aerial network planning, deployment and optimization in practice.

Appendix

A. Proof of Lemma 1

Proof. In order to facilitate calculations, we provide a two-dimensional Cartesian coordinate system, as depicted in Fig. 7. The AN projection point, denoted as $\boldsymbol{o}$, is situated at the origin of the coordinate system. The center point $\boldsymbol{u}$ of the user area is situated in the positive half of the x-axis. Additionally, conditioned on $M = m_0$, the coordinates of $\boldsymbol{u}$ is given by $(m_0, 0)$.

1) Given that $0 < m_0 < R_U - R_A$, $\mathcal{S}_{\mathcal{A}}^{'}$ is entirely contained within $\mathcal{S}_{\mathcal{U}}$, and $0 < r < R_A$. The PDF is given by $f_{R^{1)}}(r|m_0) = \frac{2r}{R_A^2}$.

Given that $R_U - R_A < m_0 < R_U$, $\mathcal{S}_{\mathcal{A}}^{'}$ and $\mathcal{S}_{\mathcal{U}}$ exhibit partial overlap. It is possible to further categorize this scenario into two distinct situations, dependent on whether the projection point falls inside the area of $\mathcal{S}_{\mathcal{U}}$. According to Fig. 7(b), it is evident that the region of overlap between $\mathcal{S}_{\mathcal{A}}^{'}$ and $\mathcal{S}_{\mathcal{U}}$ corresponds to the intersection area of two circles: one with a radius of R_A centered at the origin, and the other with a radius of R_U centered at $(m_0, 0)$. Hence, the abscissa x^* at which the two circles intersect can be expressed as $x^* = \frac{m_0^2 - R_U^2 + R_A^2}{2m_0}$.

Then the intersecting area, denoted as γ, can be expressed as

$$\begin{aligned}\gamma =& \int_{m_0 - R_U}^{x^*} 2\sqrt{R^2 - (x - m_0)^2}\mathrm{d}x + \int_{x^*}^{R_A} 2\sqrt{R_A^2 - x^2}\mathrm{d}x \\ =& R_U^2\left(\theta_2 - \frac{1}{2}\sin\left(2\theta_2\right)\right) + R_A^2\left(\varphi_2 - \frac{1}{2}\sin\left(2\varphi_2\right)\right), \end{aligned} \quad (10)$$

i.e., γ, θ_2 and φ_2 are given in the description of Lemma 1.

2) If $0 < r < R_U - m_0$ and $R_U - R_A < m_0 < R_U$, the PDF of r can be expressed as $f_{R^{2)}}(r|m_0) = \frac{2\pi r}{\gamma}$.

3) However, if $R_U - m_0 < r < R_A$ and $R_U - R_A < m_0 < R_U$, the overlapping region contains only a segment of the circle defined by the equation $x^2 + y^2 = r^2$. The abscissa

x_1^*, which represents the intersection point between the circle $x^2+y^2=r^2$ and the circle $(x-m_0)^2+y^2=R_U^2$, is given by $x_1^*=\frac{m_0^2-R_U^2+r^2}{2m_0}$.

Thus the CDF of r can be written as

$$F_{R^{3)}}(r|m_0)=\frac{1}{\gamma}\left(R_U^2\left(\theta_4-\frac{1}{2}\sin\left(2\theta_4\right)\right)+r^2\left(\varphi_3-\frac{1}{2}\sin\left(2\varphi_3\right)\right)\right), \tag{11}$$

where $\theta_4 = \arccos\left(\frac{m_0+R_U^2-r^2}{2m_0R_U}\right)$ and $\varphi_3 = \arccos\left(\frac{m_0^2-R_U^2+r^2}{2m_0r}\right)$. The corresponding PDF $f_{R^{3)}}(r|m_0)$ is then obtained.

4) Similarly, if $m_0-R_U<r<R_A$ and $R_U<m_0<R_U+R_A$, as shown in Fig. 7(c), we can easily obtain the PDF as $f_{R^{3)}}(r|m_0)$. This completes the proof. □

B. Proof of Theorem 1

Proof.

$$\begin{aligned}P_{\text{cov}}^{T-A} =&\mathbb{P}\left(\text{SINR}_1\geq T_{h_1}\right)\\ =&\mathbb{E}_{R_m}\left[\mathbb{P}\left(\text{SINR}_1\geq T_{h_1}|R_m=r_m,m_0\right)\right]\\ =&\int\int\mathbb{P}\left(\text{SINR}_1\geq T_{h_1}|R_m=r_m,m_0\right)\\ &\times f_{R_m}(r_m|m_0)\,f_M(m_0)\,\mathrm{d}r_m\,\mathrm{d}m_0.\end{aligned} \tag{12}$$

We note that $\mathbb{P}\left(\text{SINR}_1\geq T_{h_1}|R_m=r_m,m_0\right)$ satisfies:

$$\begin{aligned}&\mathbb{P}\left(\text{SINR}_1\geq T_{h_1}|R_m=r_m,m_0\right)\\ &=1-\mathbb{P}\left(|h_{T_mA}|^2\leq\frac{T_{h_1}I_T(H_A^2+r_m^2)^{\frac{\alpha_1}{2}}}{P_T}\right)\\ &\overset{(a)}{<}1-\mathbb{E}\left[\left(1-\exp\left(\frac{-\eta T_{h_1}I_T(H_A^2+r_m^2)^{\frac{\alpha_1}{2}}}{P_T}\right)\right)^{N_{TA}}\right]\\ &\overset{(b)}{=}\sum_{n=1}^{N_{TA}}(-1)^{n+1}\binom{N_{TA}}{n}\mathbb{E}_I\left[\exp\left(\frac{-n\eta T_{h_1}I_T(H_A^2+r_m^2)^{\frac{\alpha_1}{2}}}{P_T}\right)\right]\\ &\overset{(c)}{=}\sum_{n=1}^{N_{TA}}(-1)^{n+1}\binom{N_{TA}}{n}\mathbb{E}_I\left[\exp\left(-sI_T\right)\right],\end{aligned} \tag{13}$$

where (a) is a tight upper bound when N_{TA} is small [10], that is, for small N_{TA}, $\mathbb{P}\left(|h|^2<\psi\right)<\mathbb{E}\left[\left(1-\exp(-\psi\eta)\right)^{N_{TA}}\right]$ with $\eta=N_{TA}(N_{TA}!)^{-\frac{1}{N_{TA}}}$, and (b) is obtained by binomial theorem, while (c) is obtained by denoting $s=\frac{n\eta T_{h_1}(H_A^2+r_m^2)^{\frac{\alpha_1}{2}}}{P_T}$. This completes the proof. □

C. Proof of Lemma 3

Proof. Assumed that the distance denoted as R_n between the interference user and the projection point is equal to r_n. Thus, $\mathcal{L}_{I_T}(s)$ can be written as

$$\begin{aligned}\mathcal{L}_{I_T}(s)&=\mathbb{E}\left[\prod_{T_n\in\Phi_U\setminus T_m}\exp\Big(-sP_T\left|h_{T_nA}\right|^2(H_A^2+r_n^2)^{-\frac{\alpha_1}{2}}\Big)\right]\\ &=\mathbb{E}_{N_I,R_n}\Bigg[\prod_{T_n\in\Phi_U\setminus T_m}\mathbb{E}_{|h_{T_nA}|^2}\Bigg[\exp\Bigg(\left|h_{T_nA}\right|^2\\ &\qquad\times\left(-sP_T(H_A^2+r_n^2)^{-\frac{\alpha_1}{2}}\right)\Bigg)\Bigg]\Bigg]\\ &\overset{(a)}{=}\mathbb{E}_{N_I,R_n}\Bigg[\prod_{T_n\in\Phi_U\setminus T_m}\underbrace{\left(1+\frac{sP_T}{N_{TA}(H_A^2+r_n^2)^{\frac{\alpha_1}{2}}}\right)^{-N_{TA}}}_{D_2}\Bigg],\end{aligned} \tag{14}$$

where (a) is obtained by using the moment-generating function (MGF) of the normalized Gamma random variable. This completes the proof. □

References

[1] Z. Wei, Z. Meng, M. Lai, H. Wu, J. Han, and Z. Feng, "Anti-collision technologies for unmanned aerial vehicles: Recent advances and future trends," *IEEE Internet Things J.*, vol. 9, no. 10, pp. 7619–7638, May. 2022.

[2] V. V. Chetlur and H. S. Dhillon, "Downlink coverage analysis for a finite 3-D wireless network of Unmanned Aerial Vehicles," *IEEE Trans. Commun.*, vol. 65, no. 10, pp. 4543–4558, Oct. 2017.

[3] W. Yi, Y. Liu, A. Nallanathan, and G. K. Karagiannidis, "A unified spatial framework for clustered uav networks based on stochastic geometry," in *GLOBECOM 2018 (Abu Dhabi, United Arab Emirates)*, Dec. 09-13, 2018, pp. 1–6.

[4] M. Gapeyenko, V. Petrov, D. Moltchanov, S. Andreev, N. Himayat, and Y. Koucheryavy, "Flexible and reliable uav-assisted backhaul operation in 5g mmwave cellular networks," *IEEE J. Sel. Areas Commun.*, vol. 36, no. 11, pp. 2486–2496, Nov. 2018.

[5] T. Shafique, H. Tabassum, and E. Hossain, "End-to-end energy-efficiency and reliability of uav-assisted wireless data ferrying," *IEEE Trans. Commun.*, vol. 68, no. 3, pp. 1822–1837, Mar. 2020.

[6] Y. Liu, H.-N. Dai, M. Imran, and N. Nasser, "Ground-to-uav communication network: Stochastic geometry-based performance analysis," in *ICC 2021 (Montreal, QC, Canada)*, Jun. 2021, pp. 1–6.

[7] M. Afshang and H. S. Dhillon, "Fundamentals of modeling finite wireless networks using binomial point process," *IEEE Trans. Wireless Commun.*, vol. 16, no. 5, pp. 3355–3370, Mar. 2017.

[8] B. Cho, K. Koufos, and R. Jantti, "Bounding the mean interference in matérn type ii hard-core wireless networks," *IEEE Wireless Commun. Lett.*, vol. 2, no. 5, pp. 563–566, Oct. 2013.

[9] X. Zhang, B. Zhang, K. An, G. Zheng, S. Chatzinotas, and D. Guo, "Stochastic geometry-based analysis of cache-enabled hybrid satellite-aerial-terrestrial networks with non-orthogonal multiple access," *IEEE Trans. Wireless Commun.*, vol. 21, no. 2, pp. 1272–1287, Feb. 2022.

[10] H. Alzer, "On some inequalities for the incomplete gamma function," *Math. Comput.*, vol. 66, no. 218, pp. 771–778, 1997.